Environmental Controls on Tropical Mesoscale Convective System Precipitation Intensity

KATHLEEN A. SCHIRO,[a,e] SYLVIA C. SULLIVAN,[b] YI-HUNG KUO,[c] HUI SU,[a] PIERRE GENTINE,[b] GREGORY S. ELSAESSER,[d] JONATHAN H. JIANG,[a] AND J. DAVID NEELIN[c]

[a] *Jet Propulsion Laboratory, California Institute of Technology, Pasadena, California*
[b] *Department of Earth and Environmental Engineering, Columbia University, New York, New York*
[c] *Department of Atmospheric and Oceanic Sciences, University of California, Los Angeles, Los Angeles, California*
[d] *NASA Goddard Institute for Space Studies, New York, New York*

(Manuscript received 16 April 2020, in final form 1 August 2020)

ABSTRACT: Using multiple independent satellite and reanalysis datasets, we compare relationships between mesoscale convective system (MCS) precipitation intensity P_{max}, environmental moisture, large-scale vertical velocity, and system radius among tropical continental and oceanic regions. A sharp, nonlinear relationship between column water vapor and P_{max} emerges, consistent with nonlinear increases in estimated plume buoyancy. MCS P_{max} increases sharply with increasing boundary layer and lower free tropospheric (LFT) moisture, with the highest P_{max} values originating from MCSs in environments exhibiting a peak in LFT moisture near 750 hPa. MCS P_{max} exhibits strikingly similar behavior as a function of water vapor among tropical land and ocean regions. Yet, while the moisture–P_{max} relationship depends strongly on mean tropospheric temperature, it does not depend on sea surface temperature over ocean or surface air temperature over land. Other P_{max}-dependent factors include system radius, the number of convective cores, and the large-scale vertical velocity. Larger systems typically contain wider convective cores and higher P_{max}, consistent with increased protection from dilution due to dry air entrainment and reduced reevaporation of precipitation. In addition, stronger large-scale ascent generally supports greater precipitation production. Last, temporal lead–lag analysis suggests that anomalous moisture in the lower–middle troposphere favors convective organization over most regions. Overall, these statistics provide a physical basis for understanding environmental factors controlling heavy precipitation events in the tropics, providing metrics for model diagnosis and guiding physical intuition regarding expected changes to precipitation extremes with anthropogenic warming.

KEYWORDS: Convective storms/systems; Deep convection; Buoyancy; Humidity; Mesoscale systems; Convective parameterization

1. Introduction

Precipitation extremes are expected to increase in a warmer world (O'Gorman and Schneider 2009; Pendergrass and Hartmann 2014), following changes in moisture (Muller et al. 2011; Romps 2011; Fildier et al. 2017; Chen et al. 2019), larger-scale dynamics (Norris et al. 2019), and convective-scale dynamics (Emori and Brown 2005; Romps 2011; Pendergrass et al. 2016). However, climate models (GCMs), our main tools for understanding changes to the physical climate under anthropogenic warming, still have difficulty simulating basic characteristics of precipitation and clouds (e.g., Stevens and Bony 2013), due in large part to the uncertain representation of deep convection (Kim et al. 2011; Oueslati and Bellon 2013; Zhao 2014; Bernstein and Neelin 2016; Schiro et al. 2019; Kuo et al. 2020). A lack of process-level understanding of deep convection perpetuates this uncertainty in simulating changes in clouds and precipitation with anthropogenic warming. In fact, key physics defining the most intense systems in the tropics, at scales between individual convective towers and tropical cyclones, are not represented in climate models at all. This is largely because we still lack a basic understanding of how the largest, rain-producing systems in the tropics are formed and what factors most strongly control their precipitation intensity. As a result, our understanding of changes to precipitation and hydroclimatological extremes has been limited.

One of the most uncertain factors in determining changes to precipitation extremes is the unknown response of convective organization to warming (Muller and Takayabu 2020). Currently, the simplest rough estimate for changes to individual precipitation extremes is an increase of ~7% K^{-1} as would occur due to increases in moisture assuming the statistics of vertical velocity remain unchanged. However, the convective-scale dynamical contribution to this increase is highly uncertain. Some high-resolution studies find relatively small dynamical contribution under radiative–convective equilibrium (Abbott et al. 2020) while global-scale models can exhibit higher than Clausius–Clapeyron (super CC) changes with temperature in the tropics (Pall et al. 2007; Norris et al. 2019) and there is a substantial literature on super-CC scaling in observations (see, e.g., Lenderink et al. 2017). Our best estimates so far regarding changes to convective organization with warming originate from idealized modeling studies (e.g., Pendergrass et al. 2016; Coppin and Bony 2018), yet it is unclear how these results may apply to the real world. Therefore, more observations examining the physics controlling convective organization are sorely needed (Holloway et al. 2017).

[e] Current affiliation: University of Virginia, Charlottesville, Virginia.

Corresponding author: Kathleen A. Schiro, kschiro@virginia.edu

DOI: 10.1175/JAS-D-20-0111.1

In a recent study, Sullivan et al. (2019) contrasted mesoscale convective system (MCS) characteristics between El Niño and La Niña events to gauge the response of convective organization to larger-scale warming in observations. Results suggest an increase of up to 20% in convective organization across scales and other key changes in MCS characteristics, such as increasing MCS radius and MCS frequency in the central east Pacific. In addition, complementary to the results of Tan et al. (2015), Sullivan et al. (2019) found that increases in precipitation in the deep tropics can be largely attributed to an increase in MCS frequency. However, it is difficult to link current climate to future changes without first understanding the environmental controls on MCS precipitation. Moreover, it is challenging to assess future changes to precipitation extremes using GCMs that do not simulate key features of MCSs.

Most deep convection parameterization in GCMs is buoyancy based: the precipitation produced is proportional to the total amount of instability generated by grid-scale variables. This instability is given as an integral measure of the total buoyancy available to deep convection, which is estimated differently in each GCM. Ideally, such a buoyancy estimate would be consistent with observed deep convection tropics-wide, yet this has only been explicitly tested by a few studies (e.g., Suhas and Zhang 2014; Song and Zhang 2017). The fact that deep convective systems are diverse (organized, disorganized) and occur in many different regions seemingly complicates matters, though the results presented in this paper and in a few recent others (Schiro et al. 2018; Ahmed and Neelin 2018; Schiro and Neelin 2019) suggest otherwise. There is also a push to expand deep convection parameterization to include explicit features of MCSs (e.g., Moncrieff 2019), such as dynamical triggering, cold pools, and layer lifting. Here, we aim to provide guidance for development of MCS parameterization and improvement of existing buoyancy-based parameterization by presenting statistical relationships to larger-scale environmental variables generating instability and intense precipitation.

One such statistic is the strong relationship between precipitation and column water vapor (CWV) seen in observations (Bretherton et al. 2004; Peters and Neelin 2006; Neelin et al. 2009; Holloway and Neelin 2009; Sahany et al. 2012; Rushley et al. 2018; Kuo et al. 2018). It is robust across land and ocean regions (Schiro et al. 2016; Ahmed and Schumacher 2017), as well as for different seasons and times of day (Schiro and Neelin 2019). This robustness has suggested the possibility that a single buoyancy metric could realistically represent the onset and intensity of tropical deep convection in GCMs (Ahmed et al. 2020). This strong relationship is thought to result in large part from the dependence of deep convection on entrainment, whereby strong mixing with environmental air in the lower free troposphere would decrease buoyancy (Derbyshire et al. 2004; Holloway and Neelin 2009; Sahany et al. 2012; Schiro et al. 2016; Kuo et al. 2017; Schiro et al. 2018; Ahmed and Neelin 2018; Schiro and Neelin 2019). Therefore, Schiro et al. (2018) and Ahmed and Neelin (2018) suggested that a single buoyancy metric could accurately represent precipitation onset and intensity in models if sufficient mixing through a deep lower tropospheric layer (''deep-layer inflow'') is included in buoyancy calculations. At longer time scales and in steady state, this relationship is also a result of convective detrainment (Singh et al. 2019) and coupling to the boundary layer (Emanuel 2019).

Moreover, while it is expected that MCS precipitation is largely inherent to these statistics (Masunaga 2012; Ahmed and Schumacher 2015) as MCSs contribute to at least half of the total tropical rainfall and up to 90% in certain regions (Nesbitt et al. 2006), we still know very little about the environments favorable to organized convection in the tropics because of the lack of high-frequency observations. Schiro and Neelin (2019), using radar, rain gauge, and radiosonde data collected from the GoAmazon2014/5 campaign (Martin et al. 2016) suggested that organized and disorganized convection in the Amazon form in similar thermodynamic environments, specifically within environments where moisture is anomalously high in the lower free troposphere (700–900 hPa). Here, we use infrared imagery from geostationary and polar orbiting satellites to explore this dependence further by detecting MCSs, exploring environmental factors that control the intensity of precipitation they produce, and searching for clues regarding the environmental characteristics favoring the upscale growth of tropical deep convection.

In section 3, we characterize the dependence of MCS precipitation intensity on the thermodynamic environment. Results presented in section 4 isolate the contribution of precipitation from the convective and stratiform MCS regimes. Section 5 identifies dependences of MCS precipitation intensity on MCS size and large-scale dynamics. Section 6 examines preconvective environments that support convective organization. The implications of these results for improving the parameterization of convection in GCMs will then be discussed.

2. Data and methods

a. MCS detection from ISCCP data

The International Satellite Cloud Climatology Project (ISCCP) convective tracking (CT) database (https://isccp.giss.nasa.gov/CT/) is used to define MCS properties, based on a pixel-level cloud product between July 1983 and July 2008 (Rossow and Schiffer 1999; Rossow et al. 1996). The ISCCP cloud database is based upon satellite-measured radiances in the atmospheric window infrared band at $\approx 11\ \mu$m and visible band at $\approx 0.6\ \mu$m to distinguish cloudy and clear pixels. Brightness temperature calculated from these radiances identifies high clouds as being ≤ 245 K. Equating brightness temperature with cloud-top temperature (CTT) implies that the cloud acts as a blackbody to absorb all incident infrared radiation, approximately true for very opaque clouds. Cloudy pixels are then grouped into horizontal clusters at 3-hourly temporal resolution, based on unique cloud edge pixels that do not touch other clusters (Machado and Rossow 1993; Wielicki and Welch 1986). This method considers both a brightness temperature threshold of 245 K (noted above; denotes mesoscale anvil cloud) with one or

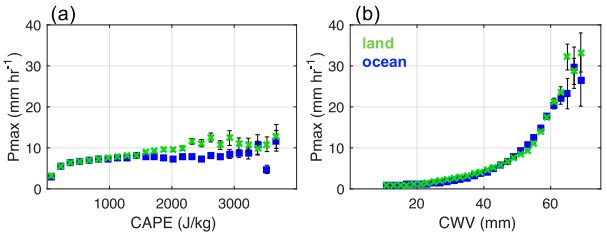

FIG. 1. Precipitation intensity in mesoscale convective systems (land and ocean) increases strongly with CWV and weakly with CAPE. The precipitation maximum P_{max} from MSWEP within the defined maximum and minimum latitude and longitude of MCS extent in the ISCCP CT database conditionally averaged as a function of coincident (a) CAPE and (b) CWV integrated from 1000 to 200 hPa. CAPE and CWV values are taken from the nearest ERA-Interim grid box to the centroid of the MCS.

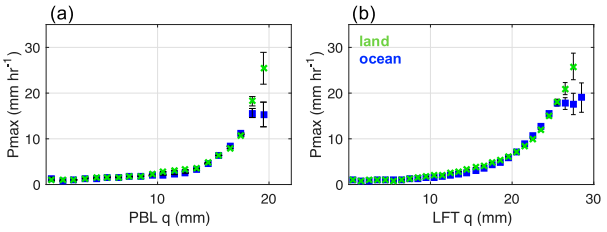

FIG. 2. Precipitation intensity in mesoscale convective systems (land and ocean) increases strongly with increasing boundary layer (PBL; 900–1000 hPa) and lower free tropospheric (LFT; 700–900 hPa) moisture. As in Fig. 1b, but separating the contributions of (a) PBL moisture and (b) LFT moisture to the statistics presented between P_{max} and total CWV in Fig. 1b.

more pixels $\leq$ 220 K (embedded deep cumulonimbus core). We have retained only systems with at least one core meeting the 220-K threshold in our study. System extent is calculated as an equivalent radius of the area covered by the pixels; that is, $r = (na/\pi)^{1/2}$, where n is the number of pixels and a is 900 km^2 for pixels with an area of 30 km by 30 km (Machado and Rossow 1993). An extent criterion of 90 km in equivalent radius (3 pixels) is enforced. A total of 727 588 systems are included in the statistics presented in Figs. 1 and 2.

To examine the contribution of stratiform and convective precipitation to the total precipitation from MCSs in section 4, we extend the above ISCCP dataset with ISCCP B1 data (https://www.ncdc.noaa.gov/gridsat/isccp-b1-info.php; Knapp 2008) to include most of the Tropical Rainfall Measurement Mission (TRMM) record to make use of the Precipitation Radar data (described below). In doing so, the criteria for MCS detection follows Mohr and Zipser (1996): systems with a brightness temperature <250 K (at least one cell < 225 K) over an area larger than 2000 km^2.

This study largely focuses on the larger-scale thermodynamic environments favorable for heavily precipitating MCSs in the tropics (30°S–30°N) and aims to build robust statistics for GCM diagnosis and parameterization development. Therefore, though we acknowledge that more recent regional convective databases are moving toward hourly or even half-hourly temporal resolution to better illustrate convective evolution and have refined MCS definitions to include precipitation thresholds (Feng et al. 2016; Roca et al. 2017), we have chosen to instead exploit the longer-term IR database from ISCCP. Newer, more sophisticated tracking algorithms being developed will, however, greatly improve our understanding of how MCSs interact with their thermodynamic environments throughout their life cycles, which will be an invaluable resource following onto the work being presented here.

b. Precipitation data

Precipitation collocated with MCSs detected by the ISCCP CT database is from the Multi-Source Weighted-Ensemble Precipitation (MSWEP) project, version 2.2, at 0.5° spatial and 3-hourly temporal resolution (Beck et al. 2017) over the same time period as the ISCCP CT database (1983–2008). MSWEP synthesizes rain gauge [Climate Prediction Center (CPC) Gauge-Based Analysis of Global Daily Precipitation and the Global Precipitation Climatology Centre] and satellite measurements (CPC morphing, Global Satellite Mapping of Precipitation, and TRMM Multisatellite Precipitation Analysis) with reanalysis data [European Centre for Medium-Range Weather Forecasting's (ECMWF) ERA-Interim and the Japanese 55-year Reanalysis]. These data are available through a repository (at www.gloh2o.org). Given the use of IR data in the ISCCP CT database and the MSWEP database, there is likely to be some overlap in detection and precipitation estimation. While this overlap would favor accurate collocation of detection and precipitation estimation, a lack of radar-based precipitation detection before the TRMM era may bias the magnitude of the precipitation estimate. As a best-estimate for maximum precipitation intensity P_{max}, we use the maximum 3-hourly precipitation within the ISCCP-CT-defined minimum and maximum latitude and longitude of MCS system extent. Since the 0.5° MSWEP grid box can include multiple convective cores, P_{max} is both a function of precipitation intensity within individual convective cores, the area covered by convective cores, and the area covered by stratiform precipitation.

We then examine the statistical relationships presented using the combined ISCCP-CT and MSWEP datasets with independent radar estimates of precipitation from the TRMM Precipitation Radar (PR). TRMM PR rain rates from the 2A25 product (https://disc.gsfc.nasa.gov/datasets/TRMM_2A25_V7/summary) are collocated with our extended ISCCP MCS database (in Figs. 5 and 6, discussed in more detail below). These data also permit further examination of separate convective and stratiform contributions to the presented statistics. The TRMM PR rain-type classifications use convective–stratiform separation methods based on vertical structure detected from the radar (Funk et al. 2013). It also considers horizontal variability of the echo (Steiner et al. 1995). The PR algorithm classifies the echoes into convective, stratiform, or other, which are then subdivided according to level of certainty based on the agreement between the horizontal and vertical methods.

c. Environmental conditions

To evaluate the local thermodynamic environment of MCSs, we use the ERA-Interim reanalysis, version 2.0,

profiles of specific humidity, temperature, and pressure from 1983 to 2008 (0.75° × 0.75°), collocated to the nearest latitude–longitude with the convective system cores. These data are publicly available (https://www.ecmwf.int/en/forecasts/datasets/archive-datasets/reanalysis-datasets/era-interim). Additionally, for examining properties of the preconvective, larger-scale environment favoring convective organization in section 6, we collocate thermodynamic profiles from the Atmospheric Infrared Sounder (AIRS level 3; https://airs.jpl.nasa.gov/data/get_data) to the MCSs detected from the ISCCP CT to the nearest latitude and longitude of the MCS. Profiles sampled lead the MCS detection by 6 h. Last, to examine the stratiform versus convective contributions to the pickup of precipitation as a function of CWV for both MCSs and non-MCS features, we use CWV from the TRMM Microwave Imager (TMI; http://www.remss.com/missions/tmi/#data_access) and consider the dependence of these statistics on temperature from the NCEP–DOE AMIP-II reanalysis.

3. The dependence of MCS precipitation intensity on moisture and buoyancy

Here, we specifically address precipitation intensity and consider thermodynamic factors that contribute most to increasing precipitation intensity in MCSs. We start by examining the relationship between precipitation production in MCSs and two commonly used bulk metrics describing the thermodynamic environment: convective available potential energy (CAPE) and CWV.

CAPE is a theoretical maximum potential energy a convective system can extract from its environment. While CAPE has been considered a poor predictor of precipitation in the tropics (Sobel et al. 2004; Yano et al. 2005; Elsaesser and Kummerow 2013; Schiro and Neelin 2019)—and the most intense convection does not always produce the most precipitation (Hamada et al. 2015)—we wonder whether CAPE scales with the maximum precipitation intensity P_{max} observed for these larger, organized convective systems. Figure 1a shows that P_{max}, the highest value within the minimum and maximum recorded latitude and longitude of the MCS at a given 3-h interval, linearly increases with increasing CAPE. Above 1000 J kg^{-1}, the correlation coefficient for ocean points is 0.33; for all points it is 0.62. However, this positive linear relationship between Pmax and CAPE is much weaker than the relationship between P_{max} and CWV shown in Fig. 1b. Precipitation accumulation, a function of rainfall intensity R and duration D ($P = RD$; Doswell et al. 1996), also exhibits a linear dependence on CAPE (not shown). One interpretation of this weak, linear dependence of P_{max} on CAPE is that while CAPE gauges the maximum potential of convective systems, the occurrence of high CAPE alone does not guarantee that the potential can be realized. The weak dependence on CAPE could also be intimately linked to weaker convective inhibition, which would permit convection to occur more frequently and discourage CAPE from "accumulating."

Insensitivity of the CAPE–P_{max} relationship shown in Fig. 1a to lead–lag analysis (not shown) suggests that the reanalysis is sampling the larger-scale convective environment rather than the large local gradients in boundary layer moisture and temperature controlling CAPE variations (e.g., Donner and Phillips 2003) likely to be present in the real world surrounding MCSs. Since we know that the thermodynamic environment can be highly variable in space and time and CAPE is a sensitive metric to sampling (e.g., Adams and Souza 2009), we acknowledge that the CAPE–P_{max} relationship in Fig. 1a may be weak as a result of smoothing across space and time scales of relevance to deep convection onset. Nevertheless, even when carefully sampling preconvective environments using field campaign data from the GoAmazon2014/5 campaign (Schiro and Neelin 2019), a weak CAPE–precipitation relationship was observed in local MCSs environments. Further work is needed to examine this relationship at smaller spatiotemporal scales and in different regions.

As we know from previous studies, precipitation is closely related to the total column moisture, with precipitation probability and intensity increasing sharply with increasing CWV (e.g., Bretherton et al. 2004; Peters and Neelin 2006; Neelin et al. 2009). This relationship has also been found to be robust across space and time scales (Schiro et al. 2016; Kuo et al. 2018). Figure 1b shows that the same is true for MCS precipitation intensity: P_{max} picks up strongly in response to increasing CWV. This is consistent with recent results from Schiro and Neelin (2019) for MCS precipitation detected using scanning S-band radar, surface rain gauge, and radiosonde data in the Amazon. Remarkably, the relationships between MCS P_{max} and CWV are nearly identical over land and ocean regions. This is consistent with recent findings by Zhang and Fueglistaler (2020), who suggested that the subcloud MSE is nearly identical for tropical deep convection over land and ocean, though in nonconvecting regions, the MSE can differ considerably. This suggests that despite regional environmental differences of these larger systems—which might control their existence, life cycle, frequency, or other detailed characteristics—the key control on precipitation intensity is simply the total amount of moisture available in the atmospheric column.

Figure 2 reproduces Fig. 1b using partial column integrals of moisture between 900 and 1000 hPa (Fig. 2a) and between 700 and 900 hPa (Fig. 2b). We loosely refer to this 900–1000-hPa layer as the boundary layer (PBL) moisture and the 700–900-hPa layer as the lower free tropospheric (LFT) moisture. Figure 2 suggests that the dependence of P_{max} on CWV results from a strong dependence of P_{max} on both the PBL and LFT moisture. This strong dependence on 700–900 hPa moisture is consistent with the results of Schiro and Neelin (2019), where similarly strong dependence was noted for MCSs over the Amazon. Powell (2019) also generally suggests a strong influence of the 700–900-hPa layer on deep convection—specifically with respect to the lapse rate—using observations from the Indo-Pacific warm pool. The P_{max} dependence on the PBL appears stronger than precipitation–PBL relations in the results of Schiro and Neelin (2019) over the Amazon, where PBL moisture is not strongly tied to an increasing probability of precipitation for either MCS or non-MCS deep convection, although a weak relationship does exist. Holloway and Neelin (2009) suggests that at Nauru (tropical west Pacific), PBL moisture is not at all related to the pickup of precipitation

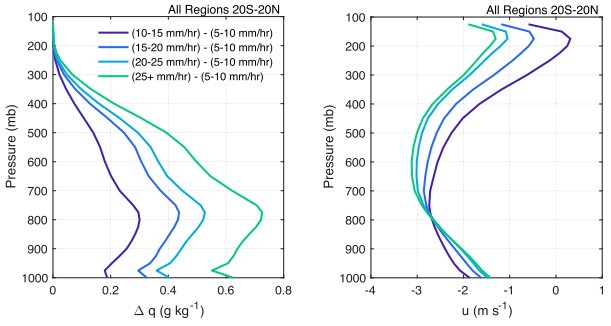

FIG. 3. Precipitation rates increase with increasing low-level vertical wind shear and column moisture, with peak moisture differences in the lower–middle troposphere. (left) Difference in specific humidity profiles for highly precipitating cases (10+ mm h^{-1}) in comparison with moderately precipitating cases (5–10 mm h^{-1}). (right) Mean of the coincident *u*-wind profiles for the highly precipitating cases.

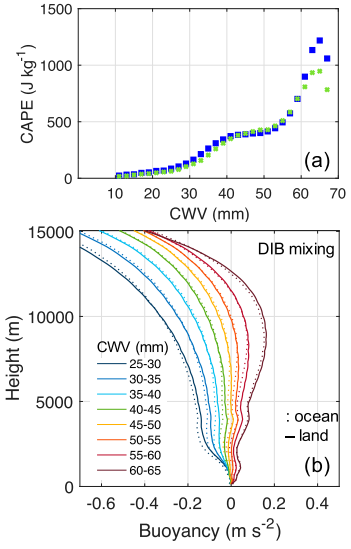

FIG. 4. Nonlinear increases in buoyancy consistent with nonlinear increases in P_{max} as a function of CWV (Fig. 1b). (a) The relationship between CAPE and CWV for land (green) and ocean (blue) MCS events. (b) Buoyancy as a function of CWV (colors) for land (solid) and ocean (dotted) MCSs estimated from an entraining plume model assuming that mixing occurs through a deep lower tropospheric layer (deep-inflow-B; Schiro et al. 2018) using ERA-Interim thermodynamic profiles collocated with the mean latitude/longitude of the MCS event.

in situ at the high time resolution being sampled. It is, therefore, possible that the *probability* of precipitation (MCS; non-MCS) is not as strongly tied to boundary layer moisture, consistent with the argument that surface-based calculations of buoyancy using nonentraining or weakly entraining plume models are inconsistent with deep convection onset (e.g., Schiro and Neelin 2019). However, the resulting precipitation *intensity*, as shown in Fig. 2a, seems to be very strongly tied to the boundary layer moisture. Credibly testing this hypothesis, however, would require higher-resolution satellite data or field campaign measurements.

Figure 3 provides additional vertical information regarding the thermodynamic structure of the environment for highly precipitating MCS (10+ mm h^{-1}), in comparison with moderately precipitating MCSs (5–10 mm h^{-1}). Figure 3a shows that the moisture difference is larger in MCS environments with higher P_{max}, as is shown in Figs. 1b and 2. The peak difference is observed in the lower free troposphere (peak ~750 hPa), consistent with the results of Schiro and Neelin (2019) tying larger convective systems to a dependence on lower free tropospheric moisture.

Additionally, since dynamics play a prominent role in controlling the amount of air entering the convective updrafts, we consider the role of wind shear in Fig. 3b. The environmental low-level shear observed in reanalysis appears rather weak, consistent with what we know about tropical MCSs in comparison to midlatitude systems, although the weaker shear relative to radiosonde data is also most probably a result of the lower resolution of these data. While examining detailed dynamical interactions requires higher-frequency observations or convection-permitting models, the increase in low-level vertical wind shear (600–1000 hPa) seen in the average *u*-wind component profiles for highly precipitating cases (as compared with low-precipitation MCSs) suggests the important role of vertical wind shear in precipitation production in tropical MCSs, consistent with observational (LeMone et al. 1998) and modeling results (Robe and Emanuel 2001; Anber et al. 2014; Cheng et al. 2020). We hypothesize that the net result of this increased shear on precipitation production is caused by modification to the properties of the inflow. It has been suggested that MCSs are characterized by a well-defined coherent layer of inflow, which can occur through a deep lower tropospheric layer (Kingsmill and Houze 1999). Modification of this inflow layer would greatly affect updraft buoyancy, condensation rates, and ultimately precipitation production. A strong dependence on both boundary layer and lower free tropospheric moisture (Fig. 2) is consistent with the "deep inflow" hypothesis.

Overall, the total moisture available to MCSs controls the buoyant energy available to support the convective updrafts and the intensity of precipitation produced. Figure 4 illustrates this point by relating CWV and two buoyancy metrics: CAPE, which is largely dependent on the thermodynamics of the level-of-origin of the plume (Fig. 4a), and another metric of buoyancy (deep-inflow B, or DIB, in Fig. 4b) that assumes $1/z$ entrainment into a plume through a deep layer extending 7 km from the surface (Schiro et al. 2018). Figure 4a suggests that CAPE and CWV may be acting together to support high P_{max} at high water vapor, but below ~55 mm, the increase in P_{max} with CWV is likely not supported by the enhancement of buoyancy from surface thermodynamics alone. Instead, as the MCS matures, convective downdrafts, cold pools, and upper level heating act to reduce CAPE. The "ledge" behavior exhibited in Fig. 4a, whereby CAPE increases between 30 and 40 mm of CWV and sharply between 55 and 65 mm (no relationship between ~40 and 50 mm) may be related to transitions between stratiform and convective precipitation within MCSs, which will be further explored in section 4. Figure 4b illustrates

that the moist lower free troposphere is also playing a major role in supporting the nonlinear increases in plume buoyancy and precipitation as a function of CWV. The buoyancy profiles suggest that below ~45 mm the atmosphere would be stable to deep convection, consistent with the location of the pickup in Fig. 1b. Appreciable rain rates below ~45 mm are primarily associated with stratiform precipitation, as will be discussed later in section 4. These relationships are remarkably similar over land and ocean regions, suggesting that buoyancy-based parameterization need not differ for land and ocean regions, if sensitive enough to PBL and LFT moisture (e.g., by including sufficient mixing through a deep lower tropospheric layer in the plume calculation; Schiro et al. 2018), despite observed differences in dynamical and microphysical convective characteristics between land and ocean regions (e.g., Liu et al. 2007; Xu and Zipser 2012; Matsui et al. 2016).

To provide a more comprehensive view of the regional characteristics of MCS precipitation, we further divide tropical land and ocean regions into 4 subregions in each category: the Indian (IND), Atlantic (ATL), east Pacific (EPac), and west Pacific (WPac) ocean regions (see Fig. A1 in the appendix: white-outlined boxes) and Maritime Continent (MC), Amazon (Amz), Congo (Cng), and west African (WAfr) continental regions (black-outlined boxes in Fig. A1). As shown in Figs. 5a–d, the largest regional differences among relationships between P_{max}, CAPE, and CWV shown in Fig. 1 occur as a function of CAPE (Fig. 5a), underscoring the problematic nature of CAPE-based closures in convection parameterizations for regional precipitation biases. In general, the Pacific Ocean regions show a weaker relationship between CAPE and P_{max} than for the Atl or IND ocean regions. Nevertheless, in all regions, the relationship between CAPE and P_{max} is weak. As is shown in Figs. 1 and 2, Figs. 5c and 5d show that the transition to strong precipitation at high CWV is equally strong for both tropical land and ocean MCSs, with interesting regional differences. Conditioning on the same bulk tropospheric temperature yields similar results (not shown). The most notable difference is for convection over the MC; differences may be due to errors in assimilating data over these regions in reanalysis or may be a result of complex island effects, sea breezes, or topographical considerations, as is suggested in Bergemann and Jakob (2016).

Both ocean and land regions (Figs. 5e and 5f, respectively) are strongly dependent on the availability of moisture in the boundary layer integrated from 1000 to 900 hPa. In general terms, the relationships between P_{max} and PBL moisture sharply transition from $P_{max} < 5\,mm\,h^{-1}$ to $P_{max} > 5\,mm\,h^{-1}$ above ~15 mm of integrated PBL moisture (Figs. 5e,f). In comparison, higher rain rates are observed at the highest LFT values, consistent with the moisture profiles conditioned on precipitation rate in Fig. 3a. The sharp transition to high precipitation ($>5\,mm\,h^{-1}$) in the LFT occurs beyond 10–15 mm of water vapor (Figs. 5g,h). We therefore conclude that MCS precipitation across all regions is tightly coupled to the availability of moisture through a deep layer of the lower troposphere, yet with some unique behavior seen for MC events.

We suspect that regional differences in P_{max} at high CWV among regions may be due to differences in conditional

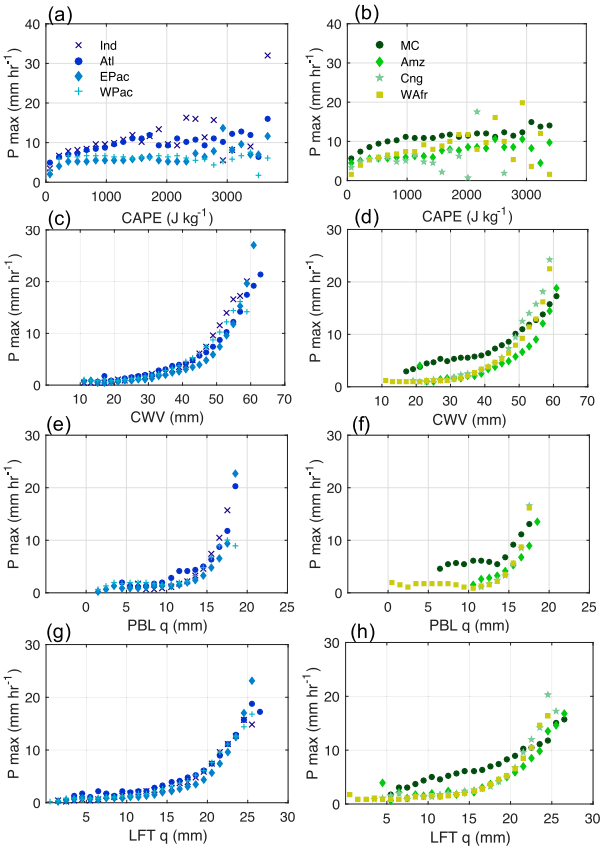

FIG. 5. Similar behavior of P_{max} as a function of integrated water vapor among land and ocean regions. As in Figs. 1 and 2, but shown for different land and ocean regions in the tropics (colors).

instability of the environment. For instance, Fig. 5d shows that for the same high CWV values, P_{max} in the Congo (Cng region) is higher than in other regions. To explore this further, Fig. 6 conditions dilute buoyancy profiles for tropical land regions, calculated by assuming entrainment occurs through a deep lower tropospheric layer 7 km deep (deep-inflow-B assumption; Schiro et al. 2018), as is done for results shown in Fig. 4b. Indeed, this result shows that the Cng region is more unstable to a deeply entraining plume throughout much of the troposphere for the same CWV relative to other regions. This result supports our hypothesis that this region experiences higher P_{max} because the greater instability supports stronger updrafts and greater precipitation production. The differences among other regions appear subtler and may be due to additional factors controlling MCS precipitation, which will be explored in the next section.

4. MCS and non-MCS convection and stratiform versus convective precipitation

In the previous section, we considered the thermodynamic factors controlling the nonlinear increase in precipitation intensity as a function of CWV. At higher CWV values, we considered that this nonlinear increase can be explained by

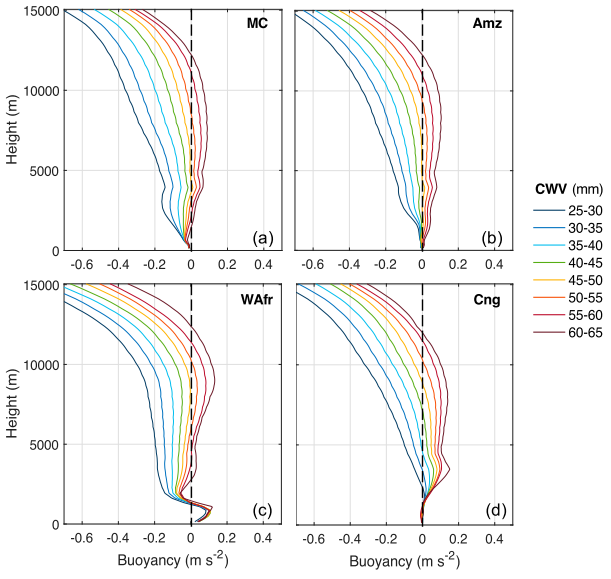

FIG. 6. Differences in buoyancy consistent with differences in precipitation intensity, particularly at high CWV (convective regime). Buoyancy profiles estimated from an entraining plume model, and conditionally averaged by CWV, corresponding to Fig. 5d for tropical land regions.

the nonlinear increase in buoyant energy available to deep convection. Yet, it is not clear whether MCS and non-MCS deep convection—and stratiform versus convective precipitation within MCSs—behave similarly as a function of their thermodynamic environments. To explore this, we employ data from the TRMM PR. Based on the convective/stratiform classification algorithm (see section 2c for details), we examine the conditional mean precipitation from MCSs as a function of CWV for four ocean basins. We focus on the common features among the four basins and defer the discussions about the regional differences to section 5.

Figure 7 shows the mean precipitation in the first column, shallow convective fraction contributing to the mean precipitation in the second column, the deeper convective fraction in the third column, and the stratiform fraction in the right most column for the tropical west Pacific (first row), east Pacific (second row), Atlantic (third row), and Indian oceans (fourth row). The abscissa of all plots is CWV relative to the critical water vapor values w_c, defined as the CWV values where a linear fit through the highest conditional mean rain rates intersects the axis (fits shown in leftmost column). This procedure yields similar dependence for different vertical-mean tropospheric temperatures (mass-weighted 200–1000 hPa) indicated by different colors of curve in the figure. The shallow convective fractions show that at ~15 mm below critical, the algorithm identifying MCSs detects shallow convection (most probably on the periphery of the MCS structure or layered within deeper cloud structures), contributing to the low rain rates seen in the conditional mean plot in the leftmost column. Between −15 and 0 mm precritical, stratiform rain fractions are highest, which increase as CWV decreases up until −15 mm precritical where the stratiform rain fractions sharply decline (peak stratiform fraction ~10 mm precritical). This suggests that convective systems of all sizes rarely exist in environments less than 15 mm below their critical CWV values.

For conditional mean precipitation from TRMM PR for MCSs and non-MCS features in the leftmost column, in all ocean basins, the MCS features seem to precipitate more strongly for the same CWV value compared with the non-MCS features. This cannot be explained by a decreased probability of observing non-MCS features in the above-critical CWV values (not shown), so we interpret this as MCS deep convective cells precipitating more strongly than non-MCS deep convective cells. One possibility for this difference is that MCSs may have more protected updraft structures than non-MCS precipitation, which will be discussed further in section 6 with relation to system radius and convective core radius. Other possibilities include additional dynamical factors like additional lift generated from cold pools or a larger fraction of cells per 25-km grid.

Figure 8 repeats the conditional mean rain rates for MCS and non-MCS features shown in the left column of Fig. 7, but additionally shows the conditional mean precipitation rates contributed by each individual rain type. It can be easily seen that the shallow convective contributions to the total conditional mean rain rate are negligible, while stratiform and convective precipitation contribute nearly equally above critical CWV. Ahmed and Schumacher (2015) and Wolding et al. (2020) also partitioned the precipitation-moisture relationship into convective and stratiform rainfall components for all systems (MCS + non-MCS combined), finding that the area of the stratiform region increased significantly with increasing CWV. Peters et al. (2009) also found a similar dependence of rain area on CWV. This could explain the similar contribution of stratiform precipitation and convective precipitation (comparing the third and rightmost columns): stratiform precipitation is less intense but occupies a greater area of a gridded average, yet convective precipitation is more intense precipitation over a less extensive area.

Another feature of these statistics worth noting is the shape of the CWV–precipitation curve (left columns; Figs. 7 and 8). There appears to be a ''ledge'' of 1 mm h^{-1} rain rates observed in the −15–0-mm subcritical range, largely resulting from stratiform precipitation. On the left side of this ledge, the precipitation rates sharply decline to 0 mm h^{-1} (<−15 mm subcritical). Interestingly, binning CAPE by CWV in Fig. 4a shows very similar ledge behavior. This may suggest that the transition between convective and stratiform regimes is largely dependent on boundary layer thermodynamics, yet Fig. 1 affirms that CAPE as a bulk quantity is not the dominant factor controlling precipitation intensity in MCSs.

Last, while there is no explicit time dimension considered in these statistics, MCS life cycle can be implied. Convective precipitation becomes more frequent and intense as CWV increases (increases in CWV with time), while stratiform precipitation represents the decay phase of convection (e.g., Houze and Betts 1981) and increases with decreasing CWV as systems move into less favorable regions and deplete

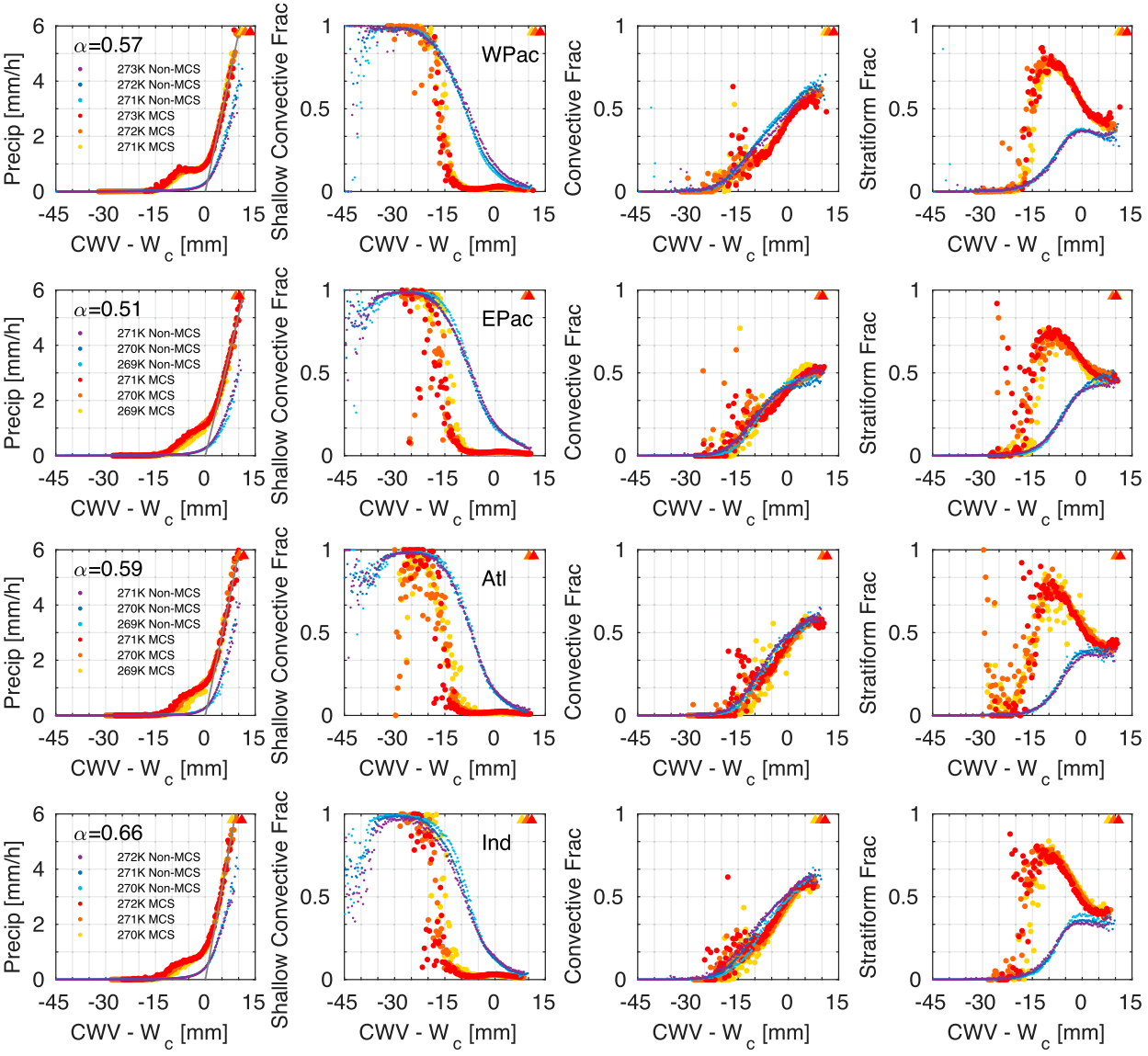

FIG. 7. Precipitation rate for MCSs (large dots) larger than non-MCS (small dots) precipitation for same column thermodynamics, with a regime shift from convective dominant to stratiform dominant below a critical threshold of water vapor w_c. (left) The TRMM 2A25 precipitation conditionally averaged by CWV for MCS and non-MCS events identified using ISCCP B1 (see section 2 text for details) as a function of CWV relative to the threshold w_c value for various tropospheric temperatures (colors; temperature data are from the NCEP–DOE AMIP-II reanalysis). (left center) the fraction of precipitation from shallow convection, (right center) the fraction of precipitation from other convective features (congestus; deep), and (right) the fraction of stratiform precipitation (using the TRMM2A23 V7 classification; Funk et al. 2013, all shown as a function of CWV $-$ w_c. Four different ocean regions are shown: the tropical (top) west Pacific, (top middle) east Pacific, (bottom middle) Atlantic, and (bottom) Indian Ocean basins as defined in Fig. A1. Slopes of the linear fit to the highest-intensity region of the curve are given by α. Triangles show the mean rescaled saturation specific humidity value (g kg^{-1}), which indicates how close to saturation a given curve lies.

moisture through precipitation. Recently, a new framework for analyzing such thermodynamic tendencies was presented by Wolding et al. (2020). Simple stochastic models have been able to reproduce basic features of these statistics considering transitions between stratiform, convective, and nonprecipitating events (Khouider et al. 2010; Stechmann and Neelin 2011, 2014; Dorrestijn et al. 2015), yet a direct observational comparison has been lacking. Therefore, these data can in turn be used to constrain parameters describing such transitions in stochastic parameterization of convection or may aid in transitioning to an explicit MCS parameterization in a GCM.

5. Other factors influencing MCS precipitation intensity

While there is a very strong relationship between precipitation intensity and moisture availability in the lower troposphere, there are subtle regional differences in the above

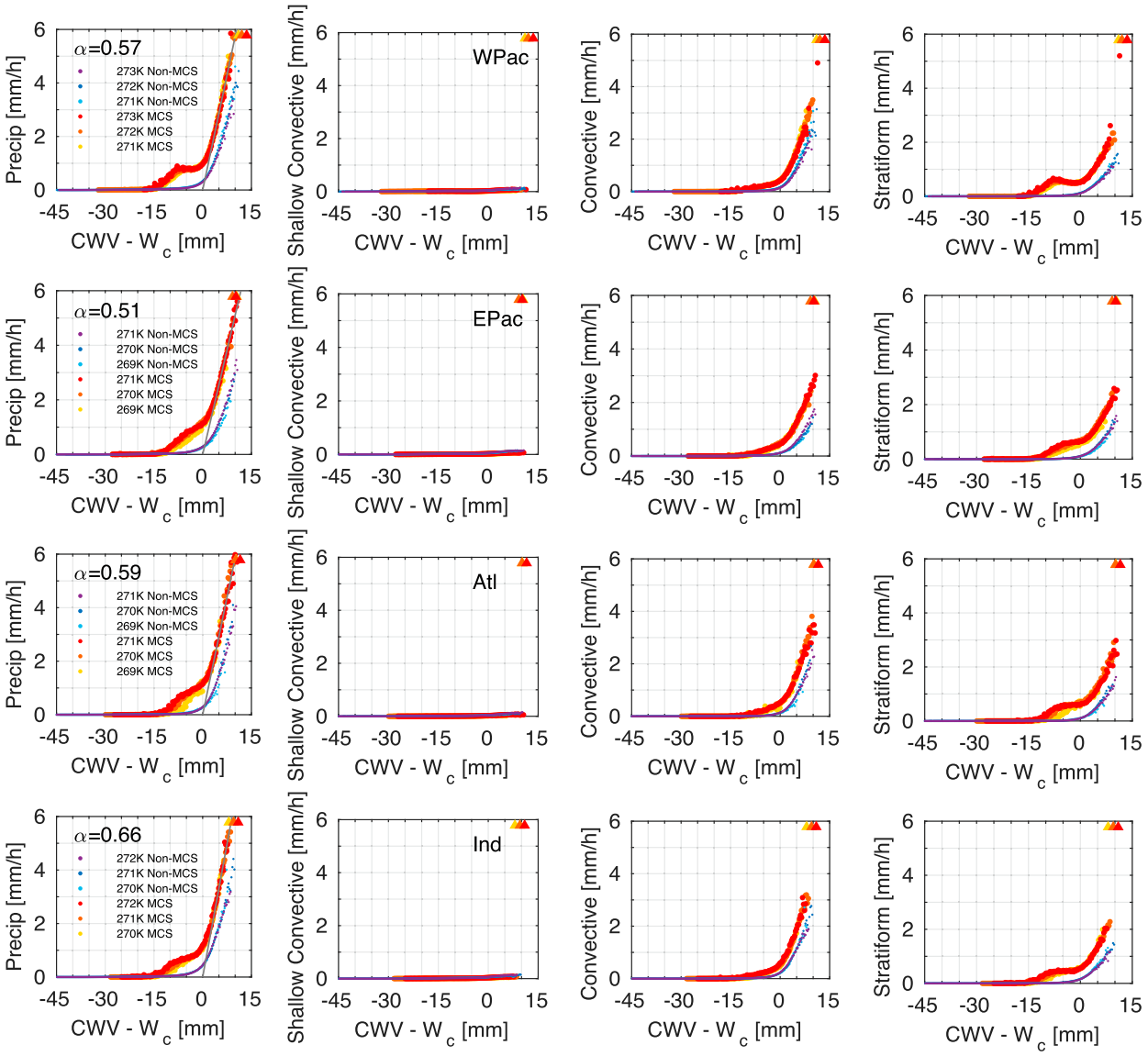

FIG. 8. Stratiform precipitation contributes most significantly to the mean precipitation at subcritical values of CWV; above critical values, convective and stratiform precipitation contribute nearly equally. As in Fig. 7, but showing the conditional mean precipitation for (left) the total precipitation, (left center) shallow convective precipitation only, (right center) convective precipitation only, and (right) stratiform precipitation.

shown statistics in sections 3 and 4 that may not be completely explained by thermodynamics or MCS phase. Therefore, we also consider how sea surface temperature, radius, and large-scale vertical velocity modify the relationship between moisture and precipitation.

Figure 9 shows the CWV–P_{max} relationship further conditioned on surface air temperature (SAT) over land only (Fig. 9a) and sea surface temperature (SST) over ocean only (Fig. 9b). The results suggest that the SST and SAT do affect the CWV–P_{max} relation for MCSs in a few noteworthy ways, but the similarity in the curves underscores the dominant role of CWV in determining the precipitation intensity of MCSs over both land and ocean. Worth noting is that the conditionally averaged P_{max} for subcritical CWV is higher for low SST/SAT than for high SST/SAT. For high CWV values, there appears to be less of a difference between high and low SST/SAT curves over ocean than over land. Over land, considering the average magnitude of all P_{max} values in CWV bins greater than 60 mm, the magnitudes of precipitation in high SAT bins is notably larger. This suggests that P_{max} in MCSs over tropical land regions do precipitate more heavily at high SAT than at low SAT. We also note that compiling these same statistics for all events (not just MCS events as is done here, including nonprecipitating events) over tropical oceans using TRMM TMI CWV and 3B42 precipitation shows nearly indistinguishable variability between curves for different SST

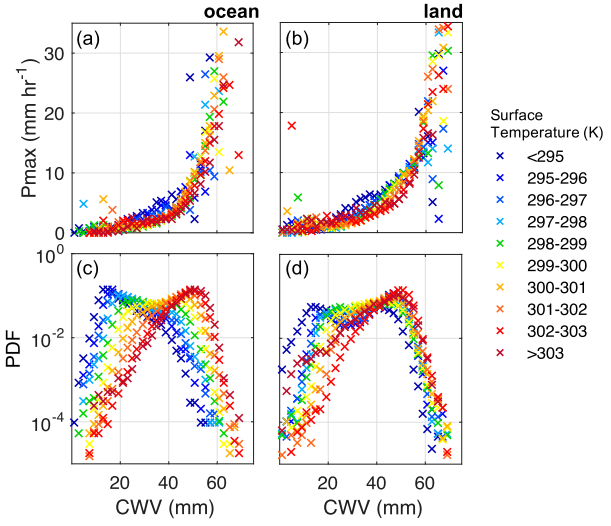

FIG. 9. The CWV–P_{max} relationship is invariant with respect to locally varying sea surface temperature (SST) and surface air temperature (SAT). (a) The CWV–P_{max} relationship further conditioned on SST over tropical ocean points (K) and (b) over tropical land points using SAT. Also shown are the PDFs of CWV conditioned on (c) SST and (d) SAT.

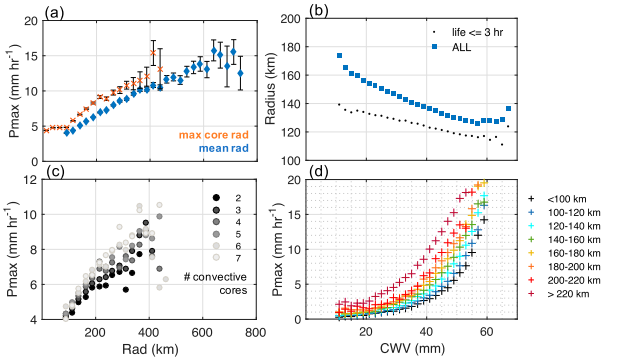

FIG. 10. Maximum precipitation intensity P_{max} increases with system radius and the number of convective cores. (a) Precipitation maximum conditionally averaged by total mean system radius (blue) and maximum convective core radius, as determined by detecting pixels with $T < 220$ K. (b) The relationship between CWV and system radius for all systems (blue squares) and systems with lifetimes ≤ 3 h (dots). (c) The relation of mean system radius vs P_{max} from (a) further conditioned on the total number of convective cores in the system. (d) The P_{max}–CWV relationship for all tropical regions shown further conditioned on system radius.

values (Neelin et al. 2009). Overall, the relationship between SST shows a much weaker relationship with P_{max} than CWV (not shown). We interpret our results in Fig. 9 as SST being generally correlated with the larger-scale thermodynamic state of the atmosphere and CWV, yet smaller-scale variations in SST do little to appreciably modify the precipitation intensity of MCSs. In other words, SST mainly determines the frequency at which CWV resides close to the critical point determining convective onset (Figs. 9c,d), rather than itself driving the onset of convection (not shown). Whether high SST/SAT encourages convective organization is a more complicated question that cannot be addressed using the data in this study.

Maximum precipitation intensity P_{max} linearly increases with increasing total system radius and convective core radius (Fig. 10a), yet the radius of the systems sampled tends to decrease with increasing CWV (Fig. 10b). The decreasing MCS radius with increasing CWV (Fig. 10b) is most probably related to the life cycle of the MCSs. As we are sampling many MCSs at different points in their convective life cycles within these statistics, the low–middle CWV values tend to be associated with more expansive cloud shields (decaying phase MCSs) than active-phase MCSs at higher CWV values. The inverse relationship between CWV and radius does not result from outliers; rather, the entire PDF of system radius within a given CWV bin shifts to lower values as CWV increases (not shown). At first glance, this result appears inconsistent with previous results (Peters et al. 2009) suggesting an increase in system radius and area with increasing CWV. However, that study considered all precipitating clusters, so the frequent occurrence of small clusters brings the conditional average radius to small values at medium to low water vapor. The statistics here are for clusters satisfying MCS criteria, including a minimum radius of 90 km, so the question asked is different—if an MCS manages to survive in a low water vapor region, how large does it tend to be? If we only include events that have lifetimes of less than 3 h this tendency for larger systems at low water vapor persists, perhaps because 3 h is sufficiently long to permit full evolution of a smaller convective system, from active convective cells to stratiform precipitation production in their wake. This may also be considered a "natural selection effect," where the only systems that survived at these low CWV values are large enough to protect their updrafts from cooler, drier outside air. There may also be frontal systems being sampled at the boundaries of the tropics. Last, larger systems may be decaying more slowly than smaller systems, which would skew the statistics toward larger values at low CWV.

Figure 10c probes the question of whether a larger number of convective cores contributes to increased precipitation intensity for a given MCS system radius. The results suggest that increasing the number of convective cells does indeed increase the mean precipitation intensity per unit area (here, the 50-km MSWEP grid), consistent with other observational and theoretical work (e.g., Craig 1996; Powell 2019). This could also be due in part to the increased detrainment and precipitation falling within stratiform regions and the complex, not fully understood interplay between convective core behavior and stratiform rainfall (e.g., Yuter and Houze 1995).

In addition to considering the areal coverage of convection, the near-linear relationship between total system radius, convective core radius, and P_{max} may also result from the fact that the convective cores within larger systems may be more protected from dilution due to dry air entrainment than in smaller systems. This would be consistent with literature surrounding decreased entrainment with increasing radii of convective plumes (e.g., Simpson 1971; de Rooy et al. 2013; Hannah 2017; Igel 2018), whereby precipitation production may be more efficient given the same CWV relative to MCSs with

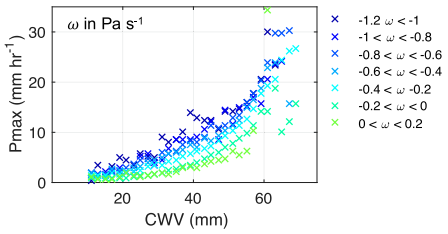

FIG. 11. Maximum precipitation intensity P_{max} increases with increasing grid-scale vertical velocity. The relationship between CWV, P_{max}, and the minimum value of ω (ERA-Interim) observed within the tropospheric column collocated with the mean latitude and longitude of the MCS.

smaller radii. Stronger convective cores may also produce more extensive anvil clouds, on average, which would result in larger MCS radii in the Fig. 10 statistics, independent of considering any effects of dilution. Figure 10d summarizes how MCSs radii affect the CWV–P_{max} statistics presented throughout.

Another factor coupled to convection and precipitation is large-scale vertical velocity. While vertical velocity in convective updrafts is largely driven by local-scale dynamical uplift and conditional instability, favorable large-scale motion in the larger-scale environment can support precipitation production. However, details of these relationships between large-scale vertical velocity and precipitation production at the convective scale remain elusive. Shown in Fig. 11, for the same CWV, if MCSs occur in regions with large-scale ascent, their P_{max} will increase with stronger upward velocity indicated by the minimum value of pressure velocity within a column ω_{min}. Additional precipitation production can result from increased convective activity or increased precipitation production. Singh et al. (2019) showed that, in cloud-resolving simulations, both the size and number of cloudy regions increased as the imposed large-scale upward motion increased. This conclusion, whereby decreased ω favors increased convective activity, likely results from the larger-scale vertical motion modifying the temperature and moisture structure of the environment, such as through moisture convergence, thus decreasing the stability and convective inhibition. However, we note the obvious caveat here that cause and effect are a bit difficult to tease out, whereby convection itself modifies the larger-scale vertical velocity, especially when considering steady-state relationships. For instance, Singh et al. (2019) uses a simple plume model to discuss how, in steady state, the relative humidity of the environment can increase with increasing large-scale upward velocity due to a weakening of subsidence drying relative to the detrainment moistening; the stability of the environment also increases. Additional work is needed to more comprehensively examine these relationships between convective-scale and larger-scale vertical motions at the short time scales sampled here, and parallels to steady-state relationships need to be carefully considered.

6. Temporal relationships between MCSs and moisture

So far, we have examined the relationship between MCS precipitation and moisture, buoyancy, and MCS structural characteristics. In this section, we more explicitly consider what large-scale thermodynamic environments may favor MCS occurrence in different regions throughout the tropics. To do so, we composite AIRS moisture profiles 6 h before an MCS was detected in a given region. We use AIRS level 3 data, which are 1° × 1° averages of all of the pixel-level data retrieved in clear-sky regions. We do so to sample only cloud-free regions that support organized convection. We then collocate this retrieval to the nearest latitude and longitude of the MCS centroid detected 6 h afterward and subtract the climatological mean moisture profile out for each region separately.

Figure 12 shows the composite soundings in MCS-favorable environments for the different ocean basins at different times of day sampled 12 h apart by AIRS. All regions except the east Pacific show increases in humidity, though the vertical structure is varied to some degree. The tropical west Pacific shows broader increases in moisture above climatological values throughout the entire troposphere, while the anomalies in the Indian ocean are top-heavy and those in the Atlantic are

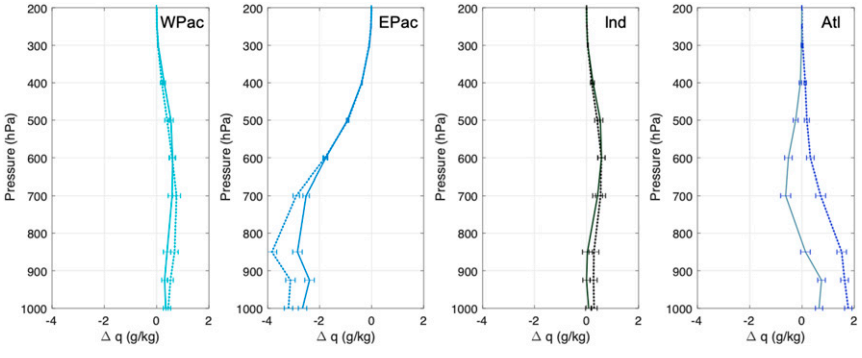

FIG. 12. Environmental moisture anomalies (AIRS) observed throughout the troposphere leading MCS detection by 6 h. Composite differences between collocated AIRS specific humidity profiles 6 h leading MCS detection and AIRS climatological mean specific humidity profiles for 1300 local time (solid) and 0100 local time (dashed) samples in (a) the west Pacific, (b) east Pacific, (c) Indian, and (d) Atlantic Ocean basins.

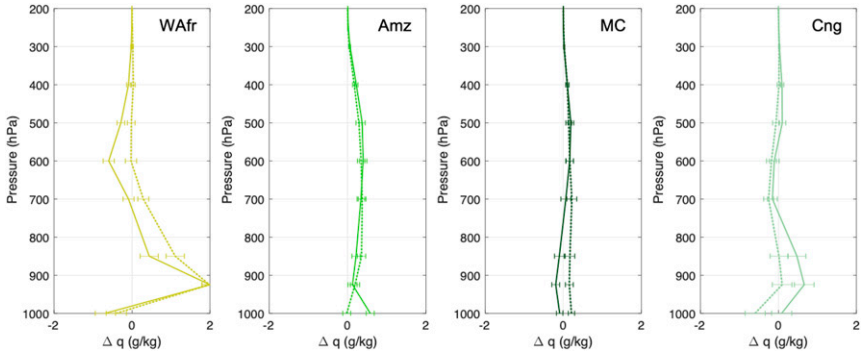

FIG. 13. Positive environmental moisture anomalies (AIRS) commonly observed throughout troposphere leading MCS detection by 6 h. As in Fig. 12, but for (a) West Africa, (b) South America, (c) the Maritime Continent, and (d) the Congo.

bottom-heavy. Different phases in the diurnal cycle can modify the amplitude of these patterns, but the overall shape of the anomalies is consistent across the diurnal cycle in all regions. For instance, the moisture anomalies in the lower atmosphere are larger during the nighttime hours (0100 LT) than during the daytime (1300 LT). In the east Pacific, the environment favorable for MCS occurrence appears to be significantly drier throughout the lower troposphere than climatological values in this region, suggesting that MCSs occur on the periphery of zones of high moisture in these regions. This is also suggested by the feature maps shown in Nesbitt et al. (2006). It is unclear whether these lower-moisture environments favor upscale growth or simply support existing organized convective systems; higher-frequency data would be necessary to make this distinction. These results, at the very least, suggest the latter. The qualitative features of these and other anomalies are reasonably robust to the lead time chosen in the analysis up to 6 h preceding MCS detection.

Figure 13 shows the departures from climatological moisture for MCS-favorable environments over tropical land regions. Over the Amazon region, there are similarly broad moisture anomalies observed throughout the troposphere, similar to the tropical west Pacific. This is broadly consistent with the results shown in Schiro et al. (2016) suggesting similar dependence of convection in these two regions on lower free tropospheric moisture. MCS-favorable moisture profiles over the MC also appear to be rather broad throughout the troposphere, though some top-heavy structure is seen during daytime hours (similar to that seen over the Indian Ocean). Overall, MC and Amz moisture anomalies are relatively small in compared with the WAfr and Cng regions.

Over west Africa, where >80% of rainfall can be attributed to MCSs (Nesbitt et al. 2006) and where some of the most intense MCSs in the world have been detected (e.g., Zipser et al. 2006), MCSs favor environments with significant moisture increases in the lower troposphere and slightly drier air in the midtroposphere. The combination of increased moisture below and decreased moisture aloft may lead to significant increases in buoyancy available to updrafts and hence more intense convection. Drier air aloft may also lead to increased downdraft strength, larger density gradients within cold pools, and greater cold pool propagation speeds (Torri et al. 2015; Torri and Kuang 2016; Gentine et al. 2016), which might support more intense convection in WAfr. Similar structures appear in the anomaly profiles observed over the Congo, though with smaller absolute magnitudes. However, whether the different profiles among different regions suggest different necessary conditions for MCSs or are simply coincidental remains to be answered and requires higher spatiotemporal coincident precipitation and cloud observations, and thermodynamic profiling.

Observing large moisture anomalies that persist for many hours leading MCS detection suggests that organized convective systems are tightly coupled to high moisture environments. This temporal lead–lag relationship has been documented before for all precipitating events (Holloway and Neelin 2010), yet it remains unclear whether high moisture environments are aiding in convection organization. Though we sample over a range of convective life cycles, the existence of MCSs in regions of high moisture, regardless of life cycle phase, suggests that the upscale growth of convection that permits persistence of precipitation for many hours is highly dependent on the moisture environment. While these data do not permit testing of mechanisms responsible for convective organization and upscale growth, and AIRS is limited by its inability to observe in cloudy scenes, the length of these data permit building robust statistics on the larger-scale dynamic and thermodynamic environments favoring the existence of convective organization.

7. Discussion

Using 25 years of MCS data products, we show that the precipitation intensity of MCSs increases strongly with increasing column moisture. The precipitation intensity relationship to water vapor, also seen separately as a function of both integrated boundary layer and lower free tropospheric moisture, is surprisingly nearly identical for land and ocean MCSs. This suggests that buoyancy-based parameterization initiating convection and determining its intensity, such as is done in conventional mass flux schemes, can appropriately treat both land and ocean precipitating systems so long as the

dependence on lower free tropospheric moisture is properly accounted for via mixing.

In comparing the relationships between precipitation intensity conditionally averaged by CAPE and CWV, we conclude that precipitation intensity does not scale as strongly with environmental instability—as estimated from undilute, pseudoadiabatic parcel ascent—as it does with column moisture. This is true over both land and ocean regions, although some regions, like west Africa and the Indian Ocean, seem to exhibit stronger sensitivity of P_{max} to variations in CAPE. This is consistent with studies suggesting that the most heavily precipitating systems are not necessarily those that occur in the most unstable environments with deep, violent updrafts (Zipser et al. 2006; Hamada et al. 2015; Singh et al. 2017). Moreover, the CWV–P_{max} relationship is invariant with respect to locally varying SST and surface air temperature. Both of these points underscore a decoupling between surface temperature and P_{max} in the tropics at the scales analyzed here. However, we find evidence that regional differences in environmental instability—as estimated from dilute parcel ascent—may contribute to regional differences in mean precipitation intensity for a given amount of column moisture.

Dynamical considerations, at both the storm scale and larger scale, are also responsible for variability in MCS precipitation intensity. Wider MCSs tend to have stronger precipitation given the same CWV, possibly due to less buoyancy reduction due to dry air entrainment in the convective cores and less reevaporation of precipitation. This is consistent with numerous theoretical studies of entrainment that have suggested a dependence of entrainment on plume radius (e.g., Morton et al. 1956; Levine 1959; Turner 1962; Lecoanet and Jeevanjee 2019). It is unsurprising that larger systems would be more protected from their environments and thus more likely to tap into available buoyant energy, yet this relationship has thus far been difficult to probe observationally given current spatiotemporal observational limitations. The total area occupied by convection will also greatly modify the observed rain rate at the resolution analyzed here (0.5°). A larger number of convective cells within a given MCS does in fact contribute to a larger observed P_{max}. These points may also explain the observed magnitude difference between non-MCS and MCS precipitation seen in Figs. 7 and 8, whereby MCS events are characterized by higher observed rain rates for the same moisture/temperature environments. Moreover, the linearity of the P_{max}–radius relationship suggests that the effect of MCS spatial characteristics on precipitation intensity may be easily parameterized. Additionally, the MCS precipitation intensity relationship to larger-scale vertical motion—whereby stronger large-scale ascent results in stronger precipitation—calls for more explicit diagnosis of interactions between larger-scale vertical motion and environmental thermodynamics in GCMs, which requires examining such interactions in greater detail in observations.

In light of recent efforts to parameterize mesoscale organization, this work suggests that the plume equation and buoyancy-based parameterization determining convective onset need not differ among convective types, so long as the instability generated is strongly related to the PBL and LFT moisture and the spatial footprint of convection is considered. Further parameterizing factors affecting MCS size and life cycle will be invaluable in improving precipitation statistics throughout the tropics. Improving the fundamentals of convective onset and the relationship between convection and its thermodynamic environment within existing parameterizations, in parallel with MCS parameterization development, could lead to significant improvements. The relationships presented in this study may also serve as useful diagnostics, not only for existing convective parameterizations but for continuing MCS parameterization development.

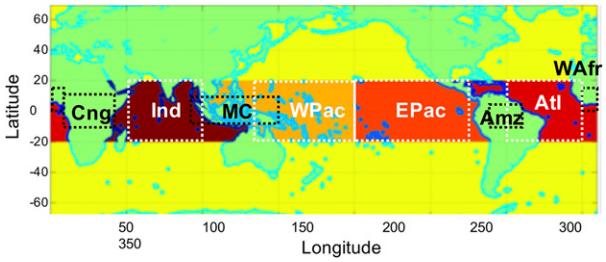

FIG. A1. Delineated regions used for the statistics presented in Figs. 5, 6, 12, and 13 (inside the black and white dotted lines) using AIRS (Figs. 12 and 13), ERA-Interim reanalysis moisture, MSWEP precipitation, and the ISCCP CT database (Figs. 5 and 6). The four regions used for Figures 7 and 8, using ISCCP B1 data, TRMM PR, and convection-type classifications over tropical ocean regions, are shaded in colors. A land mask was used in each case to isolate ocean from land pixels, derived from ERA-Interim output.

We note that these relationships presented can be considered to be most representative of interactions between convection and the larger-scale environment. Fine-scale variability in space and time, related to SST gradients, surface heterogeneities, cold pool dynamics, aerosols and other microphysical considerations will also undoubtedly influence MCS development, precipitation intensity, and life cycle.

Acknowledgments. This study was supported by the NASA ROSES NEWS, ACMAP/AST, CCST, and *Terra*/*Aqua*/*SNPP* (TASNPP) funding. The research was carried out at the Jet Propulsion Laboratory, California Institute of Technology, under contract with the National Aeronautics and Space Administration. Author Sullivan was partially supported by NSF Grant GG012658-01. Authors Kuo and Neelin were supported by NSF Project AGS-1936810, and author Elsaesser acknowledges additional support by NASA PMM RTOP WBS 573945.04.18.03.60.

Data availability statement. We gratefully acknowledge the efforts of those creating and maintaining publicly available datasets, such as the ISCCP Convective Tracking database (https://isccp.giss.nasa.gov/CT/), ERA-Interim data (https://www.ecmwf.int/en/forecasts/datasets/reanalysis-datasets/era-interim), ISCCP B1 data (https://data.nodc.noaa.gov/cgi-bin/iso?id=gov.noaa.ncdc:C00576), TRMM Precipitation Radar data and convective classification (https://pmm.nasa.gov/data-access/downloads/trmm), and MSWEP precipitation

(http://www.gloh2o.org) and TRMM TMI (http://www.remss.com/missions/tmi/#data_access) used in this study.

APPENDIX

Methods—Regional Analysis

Figure A1 delineates the regions used for the statistics presented in Figs. 5, 6, 11, and 12 (inside the black and white dotted lines) using AIRS (Figs. 11 and 12), ERA-Interim reanalysis moisture, MSWEP precipitation, and the ISCCP CT database (Figs. 5 and 6). The four regions used for Figures 7 and 8, using ISCCP B1 data, TRMM PR, and convection-type classifications over tropical ocean regions are shaded in colors. A land mask was used in each case to isolate ocean from land pixels, derived from ERA-Interim output.

REFERENCES

Abbott, T. H., T. W. Cronin, and T. Beucler, 2020: Convective dynamics and the response of precipitation extremes to warming in radiative–convective equilibrium. *J. Atmos. Sci.*, **77**, 1637–1660, https://doi.org/10.1175/JAS-D-19-0197.1.

Adams, D. K., and E. P. Souza, 2009: CAPE and convective events in the Southwest during the North American monsoon. *Mon. Wea. Rev.*, **137**, 83–98, https://doi.org/10.1175/2008MWR2502.1.

Ahmed, F., and C. Schumacher, 2015: Convective and stratiform components of the precipitation-moisture relationship. *Geophys. Res. Lett.*, **42**, 10–453, https://doi.org/10.1002/2015GL066957.

——, and ——, 2017: Geographical differences in the tropical precipitation-moisture relationship and rain intensity onset. *Geophys. Res. Lett.*, **44**, 1114–1122, https://doi.org/10.1002/2016GL071980.

——, and J. D. Neelin, 2018: Reverse engineering the tropical precipitation–buoyancy relationship. *J. Atmos. Sci.*, **75**, 1587–1608, https://doi.org/10.1175/JAS-D-17-0333.1.

——, Á. F. Adames, and J. D. Neelin, 2020: Deep convective adjustment of temperature and moisture. *J. Atmos. Sci.*, **77**, 2163–2186, https://doi.org/10.1175/JAS-D-19-0227.1.

Anber, U., S. Wang, and A. Sobel, 2014: Response of atmospheric convection to vertical wind shear: Cloud-system-resolving simulations with parameterized large-scale circulation. Part I: Specified radiative cooling. *J. Atmos. Sci.*, **71**, 2976–2993, https://doi.org/10.1175/JAS-D-13-0320.1.

Beck, H. E., A. I. J. M. Van Dijk, V. Levizzani, J. Schellekens, D. G. Miralles, B. Martens, and A. de Roo, 2017: MSWEP: 3-hourly 0.25° global gridded precipitation (1979–2015) by merging gauge, satellite, and reanalysis data. *Hydrol. Earth Syst. Sci.*, **21**, 589–615, https://doi.org/10.5194/hess-21-589-2017.

Bergemann, M., and C. Jakob, 2016: How important is tropospheric humidity for coastal rainfall in the tropics? *Geophys. Res. Lett.*, **43**, 5860–5868, https://doi.org/10.1002/2016GL069255.

Bernstein, D. N., and J. D. Neelin, 2016: Identifying sensitive ranges in global warming precipitation change dependence on convective parameters. *Geophys. Res. Lett.*, **43**, 5841–5850, https://doi.org/10.1002/2016GL069022.

Bretherton, C. S., M. E. Peters, and L. E. Back, 2004: Relationships between water vapor path and precipitation over the tropical oceans. *J. Climate*, **17**, 1517–1528, https://doi.org/10.1175/1520-0442(2004)017<1517:RBWVPA>2.0.CO;2.

Chen, G., J. Norris, J. D. Neelin, J. Lu, L. R. Leung, and K. Sakaguchi, 2019: Thermodynamic and dynamic mechanisms for hydrological cycle intensification over the full probability distribution of precipitation events. *J. Atmos. Sci.*, **76**, 497–516, https://doi.org/10.1175/JAS-D-18-0067.1.

Cheng, W. Y., D. Kim, A. Rowe, Y. Moon, and S. Wang, 2020: Mechanisms of convective clustering during a 2-day rain event in AMIE/DYNAMO. *J. Adv. Model. Earth Syst.*, **12**, e2019MS001907, https://doi.org/10.1029/2019MS001907.

Coppin, D., and S. Bony, 2018: On the interplay between convective aggregation, surface temperature gradients, and climate sensitivity. *J. Adv. Model. Earth Syst.*, **10**, 3123–3138, https://doi.org/10.1029/2018MS001406.

Craig, G. C., 1996: Dimensional analysis of a convecting atmosphere in equilibrium with external forcing. *Quart. J. Roy. Meteor. Soc.*, **122**, 1963–1967, https://doi.org/10.1002/qj.49712253611.

Derbyshire, S. H., I. Beau, P. Bechtold, J.-Y. Grandpeix, J.-M. Piriou, J.-L. Redelsperger, and P. M. M. Soares, 2004: Sensitivity of moist convection to environmental humidity. *Quart. J. Roy. Meteor. Soc.*, **130**, 3055–3079, https://doi.org/10.1256/qj.03.130.

de Rooy, W. C., and Coauthors, 2013: Entrainment and detrainment in cumulus convection: An overview. *Quart. J. Roy. Meteor. Soc.*, **139**, 1–19, https://doi.org/10.1002/qj.1959.

Donner, L. J., and V. T. Phillips, 2003: Boundary layer control on convective available potential energy: Implications for cumulus parameterization. *J. Geophys. Res.*, **108**, 4701, https://doi.org/10.1029/2003JD003773.

Dorrestijn, J., D. T. Crommelin, A. P. Siebesma, H. J. Jonker, and C. Jakob, 2015: Stochastic parameterization of convective area fractions with a multicloud model inferred from observational data. *J. Atmos. Sci.*, **72**, 854–869, https://doi.org/10.1175/JAS-D-14-0110.1.

Doswell, C. A., III, H. E. Brooks, and R. A. Maddox, 1996: Flash flood forecasting: An ingredients-based methodology. *Wea. Forecasting*, **11**, 560–581, https://doi.org/10.1175/1520-0434(1996)011<0560:FFFAIB>2.0.CO;2.

Elsaesser, G. S., and C. D. Kummerow, 2013: A multisensor observational depiction of the transition from light to heavy rainfall on subdaily time scales. *J. Atmos. Sci.*, **70**, 2309–2324, https://doi.org/10.1175/JAS-D-12-0210.1.

Emanuel, K., 2019: Inferences from simple models of slow, convectively coupled processes. *J. Atmos. Sci.*, **76**, 195–208, https://doi.org/10.1175/JAS-D-18-0090.1.

Emori, S., and S. J. Brown, 2005: Dynamic and thermodynamic changes in mean and extreme precipitation under changed climate. *Geophys. Res. Lett.*, **32**, L17706, https://doi.org/10.1029/2005GL023272.

Feng, Z., L. R. Leung, S. Hagos, R. A. Houze, C. D. Burleyson, and K. Balaguru, 2016: More frequent intense and long-lived storms dominate the springtime trend in central US rainfall. *Nat. Commun.*, **7**, 13429, https://doi.org/10.1038/ncomms13429.

Fildier, B., H. Parishani, and W. D. Collins, 2017: Simultaneous characterization of mesoscale and convective-scale tropical rainfall extremes and their dynamical and thermodynamic modes of change. *J. Adv. Model. Earth Syst.*, **9**, 2103–2119, https://doi.org/10.1002/2017MS001033.

Funk, A., C. Schumacher, and J. Awaka, 2013: Analysis of rain classifications over the tropics by version 7 of the TRMM PR 2A23 algorithm. *J. Meteor. Soc. Japan*, **91**, 257–272, https://doi.org/10.2151/jmsj.2013-302.

Gentine, P., A. Garelli, S.-B. Park, J. Nie, G. Torri, and Z. Kuang, 2016: Role of surface heat fluxes underneath cold pools. *Geophys. Res. Lett.*, **43**, 874–883, https://doi.org/10.1002/2015GL067262.

Hamada, A., Y. N. Takayabu, C. Liu, and E. J. Zipser, 2015: Weak linkage between the heaviest rainfall and tallest storms. *Nat. Commun.*, **6**, 6213, https://doi.org/10.1038/ncomms7213.

Hannah, W. M., 2017: Entrainment versus dilution in tropical deep convection. *J. Atmos. Sci.*, **74**, 3725–3747, https://doi.org/10.1175/JAS-D-16-0169.1.

Holloway, C. E., and J. D. Neelin, 2009: Moisture vertical structure, column water vapor, and tropical deep convection. *J. Atmos. Sci.*, **66**, 1665–1683, https://doi.org/10.1175/2008JAS2806.1.

——, and ——, 2010: Temporal relations of column water vapor and tropical precipitation. *J. Atmos. Sci.*, **67**, 1091–1105, https://doi.org/10.1175/2009JAS3284.1.

——, A. A. Wing, S. Bony, C. Muller, H. Masunaga, T. S. L'Ecuyer, D. D. Turner, and P. Zuidema, 2017: Observing convective aggregation. *Surv. Geophys.*, **38**, 1199–1236, https://doi.org/10.1007/s10712-017-9419-1.

Houze, R. A., Jr., and A. K. Betts, 1981: Convection in GATE. *Rev. Geophys.*, **19**, 541–576, https://doi.org/10.1029/RG019i004p00541.

Igel, M. R., 2018: Lagrangian cloud tracking and the precipitation-column humidity relationship. *Atmosphere*, **9**, 289, https://doi.org/10.3390/atmos9080289.

Khouider, B., J. Biello, and A. Majda, 2010: A stochastic multicloud model for tropical convection. *Commun. Math. Sci.*, **8**, 187–216, https://doi.org/10.4310/CMS.2010.v8.n1.a10.

Kim, D., Y. S. Jang, D. H. Kim, Y. H. Kim, M. Watanabe, F. F. Jin, and J. S. Kug, 2011: El Niño–Southern Oscillation sensitivity to cumulus entrainment in a coupled general circulation model. *J. Geophys. Res.*, **116**, D22112, https://doi.org/10.1029/2011JD016526.

Kingsmill, D. E., and R. A. Houze Jr., 1999: Kinematic characteristics of air flowing into and out of precipitating convection over the west Pacific warm pool: An airborne Doppler radar survey. *Quart. J. Roy. Meteor. Soc.*, **125**, 1165–1207, https://doi.org/10.1002/qj.1999.49712555605.

Knapp, K. R., 2008: Scientific data stewardship of international satellite cloud climatology project B1 global geostationary observations. *J. Appl. Remote Sens.*, **2**, 023548, https://doi.org/10.1117/1.3043461.

Kuo, Y. H., J. D. Neelin, and C. R. Mechoso, 2017: Tropical convective transition statistics and causality in the water vapor–precipitation relation. *J. Atmos. Sci.*, **74**, 915–931, https://doi.org/10.1175/JAS-D-16-0182.1.

——, K. A. Schiro, and J. D. Neelin, 2018: Convective transition statistics over tropical oceans for climate model diagnostics: Observational baseline. *J. Atmos. Sci.*, **75**, 1553–1570, https://doi.org/10.1175/JAS-D-17-0287.1.

——, and Coauthors, 2020: Convective transition statistics over tropical oceans for climate model diagnostics: GCM evaluation. *J. Atmos. Sci.*, **77**, 379–403, https://doi.org/10.1175/JAS-D-19-0132.1.

Lecoanet, D., and N. Jeevanjee, 2019: Entrainment in resolved, dry thermals. *J. Atmos. Sci.*, **76**, 3785–3801, https://doi.org/10.1175/JAS-D-18-0320.1.

LeMone, M. A., E. J. Zipser, and S. B. Trier, 1998: The role of environmental shear and thermodynamic conditions in determining the structure and evolution of mesoscale convective systems during TOGA COARE. *J. Atmos. Sci.*, **55**, 3493–3518, https://doi.org/10.1175/1520-0469(1998)055<3493:TROESA>2.0.CO;2.

Lenderink, G., R. Barbero, J. Loriaux, and H. Fowler, 2017: Super-Clausius–Clapeyron scaling of extreme hourly convective precipitation and its relation to large-scale atmospheric conditions. *J. Climate*, **30**, 6037–6052, https://doi.org/10.1175/JCLI-D-16-0808.1.

Levine, J., 1959: Spherical vortex theory of bubble-like motion in cumulus clouds. *J. Meteor.*, **16**, 653–662, https://doi.org/10.1175/1520-0469(1959)016<0653:SVTOBL>2.0.CO;2.

Liu, C., E. J. Zipser, and S. W. Nesbitt, 2007: Global distribution of tropical deep convection: Different perspectives from TRMM infrared and radar data. *J. Climate*, **20**, 489–503, https://doi.org/10.1175/JCLI4023.1.

Machado, L. A. T., and W. B. Rossow, 1993: Structural characteristics and radiative properties of tropical cloud clusters. *Mon. Wea. Rev.*, **121**, 3234–3260, https://doi.org/10.1175/1520-0493(1993)121<3234:SCARPO>2.0.CO;2.

Martin, S. T., and Coauthors, 2016: Introduction: Observations and modeling of the Green Ocean Amazon (GoAmazon2014/5). *Atmos. Chem. Phys.*, **16**, 4785–4797, https://doi.org/10.5194/acp-16-4785-2016.

Masunaga, H., 2012: Short-term versus climatological relationship between precipitation and tropospheric humidity. *J. Climate*, **25**, 7983–7990, https://doi.org/10.1175/JCLI-D-12-00037.1.

Matsui, T., J. D. Chern, W. K. Tao, S. Lang, M. Satoh, T. Hashino, and T. Kubota, 2016: On the land–ocean contrast of tropical convection and microphysics statistics derived from TRMM satellite signals and global storm-resolving models. *J. Hydrometeor.*, **17**, 1425–1445, https://doi.org/10.1175/JHM-D-15-0111.1.

Mohr, K. I., and E. J. Zipser, 1996: Mesoscale convective systems defined by their 85-GHz ice scattering signature: Size and intensity comparison over tropical oceans and continents. *Mon. Wea. Rev.*, **124**, 2417–2437, https://doi.org/10.1175/1520-0493(1996)124<2417:MCSDBT>2.0.CO;2.

Moncrieff, M. W., 2019: Toward a dynamical foundation for organized convection parameterization in GCMs. *Geophys. Res. Lett.*, **46**, 14 103–14 108, https://doi.org/10.1029/2019GL085316.

Morton, B. R., G. Taylor, and J. S. Turner, 1956: Turbulent gravitational convection from maintained and instantaneous sources. *Proc. Roy. Soc. London*, **234A**, 1–2, https://doi.org/10.1098/rspa.1956.0011.

Muller, C., and Y. Takayabu, 2020: Response of precipitation extremes to warming: What have we learned from theory and idealized cloud-resolving simulations, and what remains to be learned? *Environ. Res. Lett.*, **15**, 035001, https://doi.org/10.1088/1748-9326/ab7130.

——, P. A. O'Gorman, and L. E. Back, 2011: Intensification of precipitation extremes with warming in a cloud-resolving model. *J. Climate*, **24**, 2784–2800, https://doi.org/10.1175/2011JCLI3876.1.

Neelin, J. D., O. Peters, and K. Hales, 2009: The transition to strong convection. *J. Atmos. Sci.*, **66**, 2367–2384, https://doi.org/10.1175/2009JAS2962.1.

Nesbitt, S. W., R. Cifelli, and S. A. Rutledge, 2006: Storm morphology and rainfall characteristics of TRMM precipitation features. *Mon. Wea. Rev.*, **134**, 2702–2721, https://doi.org/10.1175/MWR3200.1.

Norris, J., G. Chen, and J. D. Neelin, 2019: Thermodynamic versus dynamic controls on extreme precipitation in a warming climate from the Community Earth System Model Large Ensemble. *J. Climate*, **32**, 1025–1045, https://doi.org/10.1175/JCLI-D-18-0302.1.

O'Gorman, P. A., and T. Schneider, 2009: The physical basis for increases in precipitation extremes in simulations of 21st-century climate change. *Proc. Natl. Acad. Sci. USA*, **106**, 14 773–14 777, https://doi.org/10.1073/pnas.0907610106.

Oueslati, B., and G. Bellon, 2013: Convective entrainment and large-scale organization of tropical precipitation: Sensitivity of

the CNRM-CM5 hierarchy of models. *J. Climate*, **26**, 2931–2946, https://doi.org/10.1175/JCLI-D-12-00314.1.

Pall, P., M. R. Allen, and D. A. Stone, 2007: Testing the Clausius-Clapeyron constraint on changes in extreme precipitation under CO_2 warming. *Climate Dyn.*, **28**, 351–363, https://doi.org/10.1007/s00382-006-0180-2.

Pendergrass, A. G., and D. L. Hartmann, 2014: Changes in the distribution of rain frequency and intensity in response to global warming. *J. Climate*, **27**, 8372–8383, https://doi.org/10.1175/JCLI-D-14-00183.1.

——, K. A. Reed, and B. Medeiros, 2016: The link between extreme precipitation and convective organization in a warming climate: Global radiative-convective equilibrium simulations. *Geophys. Res. Lett.*, **43**, 11 445–11 452, https://doi.org/10.1002/2016GL071285.

Peters, O., and J. D. Neelin, 2006: Critical phenomena in atmospheric precipitation. *Nat. Phys.*, **2**, 393–396, https://doi.org/10.1038/nphys314.

——, ——, and S. W. Nesbitt, 2009: Mesoscale convective systems and critical clusters. *J. Atmos. Sci.*, **66**, 2913–2924, https://doi.org/10.1175/2008JAS2761.1.

Powell, S. W., 2019: Observing possible thermodynamic controls on tropical marine rainfall in moist environments. *J. Atmos. Sci.*, **76**, 3737–3751, https://doi.org/10.1175/JAS-D-19-0144.1.

Robe, F. R., and K. A. Emanuel, 2001: The effect of vertical wind shear on radiative–convective equilibrium states. *J. Atmos. Sci.*, **58**, 1427–1445, https://doi.org/10.1175/1520-0469(2001)058<1427:TEOVWS>2.0.CO;2.

Roca, R., T. Fiolleau, and D. Bouniol, 2017: A simple model of the life cycle of mesoscale convective systems cloud shield in the tropics. *J. Climate*, **30**, 4283–4298, https://doi.org/10.1175/JCLI-D-16-0556.1.

Romps, D. M., 2011: Response of tropical precipitation to global warming. *J. Atmos. Sci.*, **68**, 123–138, https://doi.org/10.1175/2010JAS3542.1.

Rossow, W. B., and R. A. Schiffer, 1999: Advances in understanding clouds from ISCCP. *Bull. Amer. Meteor. Soc.*, **80**, 2261–2288, https://doi.org/10.1175/1520-0477(1999)080<2261:AIUCFI>2.0.CO;2.

——, A. W. Walker, D. E. Beuschel, and M. D. Roiter, 1996: International Satellite Cloud Climatology Project (ISCCP) documentation of new cloud datasets. World Climate Research Programme Rep. WMO/TD-737, 115 pp.

Rushley, S. S., D. Kim, C. S. Bretherton, and M.-S. Ahn, 2018: Reexamining the nonlinear moisture-precipitation relationship over the tropical oceans. *Geophys. Res. Lett.*, **45**, 1133–1140, https://doi.org/10.1002/2017GL076296.

Sahany, S., J. D. Neelin, K. Hales, and R. B. Neale, 2012: Temperature–moisture dependence of the deep convective transition as a constraint on entrainment in climate models. *J. Atmos. Sci.*, **69**, 1340–1358, https://doi.org/10.1175/JAS-D-11-0164.1.

Schiro, K. A., and J. D. Neelin, 2019: Deep convective organization, moisture vertical structure, and convective transition using deep-inflow mixing. *J. Atmos. Sci.*, **76**, 965–987, https://doi.org/10.1175/JAS-D-18-0122.1.

——, ——, D. K. Adams, and B. R. Lintner, 2016: Deep convection and column water vapor over tropical land versus tropical ocean: A comparison between the Amazon and the tropical western Pacific. *J. Atmos. Sci.*, **73**, 4043–4063, https://doi.org/10.1175/JAS-D-16-0119.1.

——, F. Ahmed, S. E. Giangrande, and J. D. Neelin, 2018: GoAmazon2014/5 campaign points to deep-inflow approach to deep convection across scales. *Proc. Natl. Acad. Sci. USA*, **115**, 4577–4582, https://doi.org/10.1073/pnas.1719842115.

——, H. Su, Y. Wang, B. Langenbrunner, J. H. Jiang, and J. D. Neelin, 2019: Relationships between tropical ascent and high cloud fraction changes with warming revealed by perturbation physics experiments in CAM5. *Geophys. Res. Lett.*, **46**, 10 112–10 121, https://doi.org/10.1029/2019GL083026.

Simpson, J., 1971: On cumulus entrainment and one-dimensional models. *J. Atmos. Sci.*, **28**, 449–455, https://doi.org/10.1175/1520-0469(1971)028<0449:OCEAOD>2.0.CO;2.

Singh, M. S., Z. Kuang, E. D. Maloney, W. M. Hannah, and B. O. Wolding, 2017: Increasing potential for intense tropical and subtropical thunderstorms under global warming. *Proc. Natl. Acad. Sci. USA*, **114**, 11 657–11 662, https://doi.org/10.1073/pnas.1707603114.

——, R. A. Warren, and C. Jakob, 2019: A steady-state model for the relationship between humidity, instability, and precipitation in the tropics. *J. Adv. Model. Earth Syst.*, **11**, 3973–3994, https://doi.org/10.1029/2019MS001686.

Sobel, A. H., S. E. Yuter, C. S. Bretherton, and G. N. Kiladis, 2004: Large-scale meteorology and deep convection during TRMM KWAJEX. *Mon. Wea. Rev.*, **132**, 422–444, https://doi.org/10.1175/1520-0493(2004)132<0422:LMADCD>2.0.CO;2.

Song, F., and G. J. Zhang, 2017: Improving trigger functions for convective parameterization schemes using GOAmazon observations. *J. Climate*, **30**, 8711–8726, https://doi.org/10.1175/JCLI-D-17-0042.1.

Stechmann, S. N., and J. D. Neelin, 2011: A stochastic model for the transition to strong convection. *J. Atmos. Sci.*, **68**, 2955–2970, https://doi.org/10.1175/JAS-D-11-028.1.

——, and ——, 2014: First-passage-time prototypes for precipitation statistics. *J. Atmos. Sci.*, **71**, 3269–3291, https://doi.org/10.1175/JAS-D-13-0268.1.

Steiner, M., R. A. Houze Jr., and S. E. Yuter, 1995: Climatological characterization of three-dimensional storm structure from operational radar and rain gauge data. *J. Appl. Meteor.*, **34**, 1978–2007, https://doi.org/10.1175/1520-0450(1995)034<1978:CCOTDS>2.0.CO;2.

Stevens, B., and S. Bony, 2013: What are climate models missing? *Science*, **340**, 1053–1054, https://doi.org/10.1126/science.1237554.

Suhas, E., and G. J. Zhang, 2014: Evaluation of trigger functions for convective parameterization schemes using observations. *J. Climate*, **27**, 7647–7666, https://doi.org/10.1175/JCLI-D-13-00718.1.

Sullivan, S. C., K. A. Schiro, C. Stubenrauch, and P. Gentine, 2019: The response of tropical organized convection to El Niño warming. *J. Geophys. Res. Atmos.*, **124**, 8481–8500, https://doi.org/10.1029/2019JD031026.

Tan, J., C. Jakob, W. B. Rossow, and G. Tselioudis, 2015: Increases in tropical rainfall driven by changes in frequency of organized deep convection. *Nature*, **519**, 451–454, https://doi.org/10.1038/nature14339.

Torri, G., and Z. Kuang, 2016: Rain evaporation and moist patches in tropical boundary layers. *Geophys. Res. Lett.*, **43**, 9895–9902, https://doi.org/10.1002/2016GL070893.

——, ——, and Y. Tian, 2015: Mechanisms for convection triggering by cold pools. *Geophys. Res. Lett.*, **42**, 1943–1950, https://doi.org/10.1002/2015GL063227.

Turner, J. S., 1962: The 'starting plume' in neutral surroundings. *J. Fluid Mech.*, **13**, 356–368, https://doi.org/10.1017/S0022112062000762.

Wielicki, B. A., and R. M. Welch, 1986: Cumulus cloud properties derived using Landsat satellite data. *J. Climate Appl. Meteor.*, **25**, 261–276, https://doi.org/10.1175/1520-0450(1986)025<0261:CCPDUL>2.0.CO;2.

Wolding, B., J. Dias, G. Kiladis, F. Ahmed, S. W. Powell, E. Maloney, and M. Branson, 2020: Interactions between moisture and tropical convection. Part I: The coevolution of moisture and convection. *J. Atmos. Sci.*, **77**, 1783–1799, https://doi.org/10.1175/JAS-D-19-0225.1.

Xu, W., and E. J. Zipser, 2012: Properties of deep convection in tropical continental, monsoon, and oceanic rainfall regimes. *Geophys. Res. Lett.*, **39**, L07802, https://doi.org/10.1029/2012GL051242.

Yano, J. I., J. P. Chaboureau, and F. Guichard, 2005: A generalization of CAPE into potential-energy convertibility. *Quart. J. Roy. Meteor. Soc.*, **131**, 861–875, https://doi.org/10.1256/qj.03.188.

Yuter, S. E., and R. A. Houze Jr., 1995: Three-dimensional kinematic and microphysical evolution of Florida cumulonimbus. Part III: Vertical mass transport, mass divergence, and synthesis. *Mon. Wea. Rev.*, **123**, 1964–1983, https://doi.org/10.1175/1520-0493(1995)123<1964:TDKAME>2.0.CO;2.

Zhang, Y., and S. Fueglistaler, 2020: How tropical convection couples high moist static energy over land and ocean. *Geophys. Res. Lett.*, **47**, e2019GL086387, https://doi.org/10.1029/2019GL086387.

Zhao, M., 2014: An investigation of the connections among convection, clouds, and climate sensitivity in a global climate model. *J. Climate*, **27**, 1845–1862, https://doi.org/10.1175/JCLI-D-13-00145.1.

Zipser, E. J., D. J. Cecil, C. Liu, S. W. Nesbitt, and D. P. Yorty, 2006: Where are the most intense thunderstorms on Earth? *Bull. Amer. Meteor. Soc.*, **87**, 1057–1072, https://doi.org/10.1175/BAMS-87-8-1057.